Nonlocal metasurface for dark-field edge emission

Yao, Jin; Hsu, Wei-Lun; Liang, Yao; Lin, Rong; Chen, Mu Ku ; Tsai, Din Ping

Published in:
Science Advances

Published: 01/04/2024

Document Version:
Final Published version, also known as Publisher's PDF, Publisher's Final version or Version of Record

Published version (DOI):
10.1126/sciadv.adn2752

Publication details:
Yao, J., Hsu, W.-L., Liang, Y., Lin, R., Chen, M. K., & Tsai, D. P. (2024). Nonlocal metasurface for dark-field edge emission. *Science Advances*, *10*(16), Article eadn2752. https://doi.org/10.1126/sciadv.adn2752

OPTICS

Nonlocal metasurface for dark-field edge emission

Jin Yao[1], Wei-Lun Hsu[2], Yao Liang[1], Rong Lin[1], Mu Ku Chen[1,3,4]*, Din Ping Tsai[1,3,4]*

Nonlocal effects originating from interactions between neighboring meta-atoms introduce additional degrees of freedom for peculiar characteristics of metadevices, such as enhancement, selectivity, and spatial modulation. However, they are generally difficult to manipulate because of the collective responses of multiple meta-atoms. Here, we experimentally demonstrate the nonlocal metasurface to realize the spatial modulation of dark-field emission. Plasmonic asymmetric split rings (ASRs) are designed to simultaneously excite local dipole resonance and nonlocal quasi-bound states in the continuum and spatially extended modes. With one type of unit, nonlocal effects are tailored by varying array periods. ASRs at the metasurface's edge lack sufficient interactions, resulting in stronger dark-field scattering and thus edge emission properties of the metasurface. Pixel-level spatial control is demonstrated by simply erasing some units, providing more flexibility than conventional local metasurfaces. This work paves the way for manipulating nonlocal effects and facilitates applications in optical trapping and sorting at the nanoscale.

INTRODUCTION

Metasurfaces comprising artificially customized meta-atoms have become compact and flexible tools for tailoring light-matter interactions at the nanoscale (*1*). Interactions between adjacent meta-atoms are a critical factor in determining the performances of metadevices, introducing additional degrees of freedom for light manipulation and enhancement (*2*, *3*). Local modes, such as localized surface plasmon resonances in plasmonic nanoparticles and localized Mie-type resonances in dielectric nanoresonators, are individual responses of the single meta-atom at a certain location (*4*, *5*). This capability provides opportunities for independent control of each meta-atom, enabling substantial applications in broadband and tunable wavefront shaping (*6*–*8*), sensing (*9*, *10*), multimodal perceptions (*11*, *12*), nonlinear generation (*13*), and quantum sources (*14*–*16*).

To provide more functionalities or overcome some challenges of metadevices, additional degrees of freedom are important. Compared with local metasurfaces, nonlocal effects introduce an additional degree of freedom of interactions between neighboring meta-atoms, which are beneficial for various peculiar characteristics, such as enhancement, selectivity, and spatial modulation (*17*–*21*). Nonlocal modes can be generated by reducing the distance between meta-atoms to generate their near-field coupling or enlarging the array period to involve the spatially extended modes such as propagating surface plasmon polaritons (SPPs) (*22*–*24*), surface lattice resonances (*25*, *26*), and guide-mode resonances (*27*, *28*), which have been widely used in nonlinear generation (*29*, *30*), thermal radiation (*31*), optical computing (*32*), and eye tracking (*33*). Integrating both local and nonlocal effects, nonlocal metasurfaces have also been demonstrated to achieve both spatial and spectral wavefront shaping exceeding local metasurfaces (*34*–*37*). Recently, bound states in the continuum (BICs), nonradiative states with infinite confinement lifetimes, have emerged as efficient candidates to tailor nonlocal effects (*38*). By breaking symmetry in parameter and momentum spaces or destructive mode coupling to generate the leaky quasi-BIC (q-BIC), a finite high quality factor (Q-factor) can be achieved, providing potential for tailoring near-field enhancement and far-field radiation (*39*–*42*). However, because of considerations of meta-atom's individual and collective responses, as well as their interactions, nonlocal effects are generally difficult to manipulate, especially for flexible control up to the pixel level (*43*). In addition, previous works mainly focused on the excellent performances of nonlocal metasurfaces in the bright field, and the nonlocal effects have not been effectively used to manipulate the dark-field properties.

In this work, we experimentally demonstrate a plasmonic nonlocal metasurface and its dark-field edge emission. The asymmetric split ring (ASR) (*19*, *44*, *45*) is carefully designed to excite local dipole resonances and nonlocal resonances such as q-BIC, SPP, and Wood's anomaly (WA) modes and then generate coupling between them. First, we verify the optical responses of the metasurface under normal lighting in the bright field experimentally. In the dark field with focused oblique incidence, by varying the array period, the coupled q-BIC can be controlled to suppress the far-field scattering and tailor the phase difference between adjacent ASRs for the transverse electric (TE) wave, while SPP and WA modes contribute more to transverse magnetic (TM) waves. According to the nonlocal response of these resonances, the meta-atoms on the metasurface edge lack efficient interactions from adjacent ones, resulting in a larger scattering and thus the edge emission property. More ASR arrangements with a central square or some random units further demonstrate the potential of our design for flexible light manipulation up to pixel level.

RESULTS

Optical responses in the bright field

Figure 1A depicts a schematic diagram of dark-field edge emission from nonlocal metasurfaces. By manipulating the nonlocal effect, the meta-atoms at the edge lack interactions with adjacent ones. Their resonances capable of suppressing scattering cannot be efficiently excited, resulting in a strong far-field scattering in the dark field. The building block, integrated-resonant unit (IRU), is composed of a 50-nm gold film perforated with an ASR structure, which

[1]Department of Electrical Engineering, City University of Hong Kong, Kowloon, Hong Kong SAR, China. [2]Department of Optics and Photonics, National Central University, Taoyuan 320371, Taiwan. [3]Centre for Biosystems, Neuroscience, and Nanotechnology, City University of Hong Kong, Kowloon, Hong Kong SAR, China. [4]State Key Laboratory of Terahertz and Millimeter Waves, City University of Hong Kong, Kowloon, Hong Kong SAR, China.
*Corresponding author. Email: mkchen@cityu.edu.hk (M.K.C.); dptsai@cityu.edu.hk (D.P.T.)

is placed on the silica substrate. Figure 1 (B and D) gives the scanning electron microscopy (SEM) images of fabricated samples with array periods $P = 300$ and 500 nm. With the normal illumination of *y*-polarized light, their transmission spectra in the bright field are shown in Fig. 1 (C and E). Two periods can both excite two resonances in the desired wavelength range. Resonant wavelengths and spectral shapes of experimental and simulated results can match with each other. The characteristic of dual resonances provides the possibility for the manipulation of far-field scattering by effectively tailoring their nonlocality and coupling.

Design of the ASR in the dark field

To elaborate on the design principle of the proposed ASR, its dark-field optical responses are given in Fig. 2. With the oblique incidence of average angle 61° according to the dark-field objective with a numerical aperture of 0.9, Fig. 2 (A and B) gives simulated reflection and absorption spectra as a function of period P under TE incidence. For the definition of oblique illumination, there exists an azimuth angle difference of 90° between TE and TM waves. TE wave will have E_y, H_x, and H_z components, and TM wave will have E_y, E_z, and H_x components. Two resonances, q-BIC mode and dipole resonance can be observed according to a narrowband Fano-like peak (red dashed line) and a wideband dip (blue dashed line) in reflection spectra, respectively, as well as the corresponding peaks in the absorption spectra. Relatively weak SPP and WA modes (green dashed line) can be distinguished by the abrupt shifts of reflection and absorption spectra, whose resonant wavelengths have linear relations with the array period can also be found, described as (*46*)

$$\mathbf{k}_0 \sin\theta \pm i\mathbf{G}_x \pm j\mathbf{G}_y = \mathbf{k}_{\mathrm{SPP/WA}} \tag{1}$$

where i and j are the grating orders for the reciprocal lattice vectors $\mathbf{G}_x$ and $\mathbf{G}_y$ ($|\mathbf{G}_x| = |\mathbf{G}_y| = 2\pi/P$, P is the array period), θ is the incidence angle from air, and $\mathbf{k}_0$ is the wave vector of the incident light. The wave vectors of SPP and WA are (*46*)

$$|\mathbf{k}_{\mathrm{SPP}}| = |\mathbf{k}_0| \sqrt{\frac{\varepsilon_m \varepsilon_d}{\varepsilon_m + \varepsilon_d}} \tag{2}$$

$$|\mathbf{k}_{\mathrm{WA}}| = |\mathbf{k}_0| \sqrt{\varepsilon_d} \tag{3}$$

where ε_m and ε_d are the dielectric constants of the metal and surrounding medium, respectively. When period $P = 415$ nm, influenced by the SPP and WA modes, the coupling effect between q-BIC mode and dipole resonance produces the destructive interference and thus the nonradiative BIC mode at the wavelength of ~1000 nm, as shown in Fig. 2B. Figure 2C gives magnetic field H_z distributions of two resonances at corresponding resonant wavelengths. Four positive and negative hotspots inside the ASR exhibit the quadrupole responses of q-BIC, while the dipole resonance indicates two hotspots in opposite directions. The difference between field distributions of q-BICs for two periods is caused by the coupling with the dipole resonance. More electromagnetic field distributions can be found in fig. S7 in the Supplementary Materials. The intrinsic property of BIC can be further verified by the dependences of Q-factors on geometric parameters in Fig. 2D. By varying the period P to deviate from 415 nm, the nonradiative BIC is transformed into the leaky

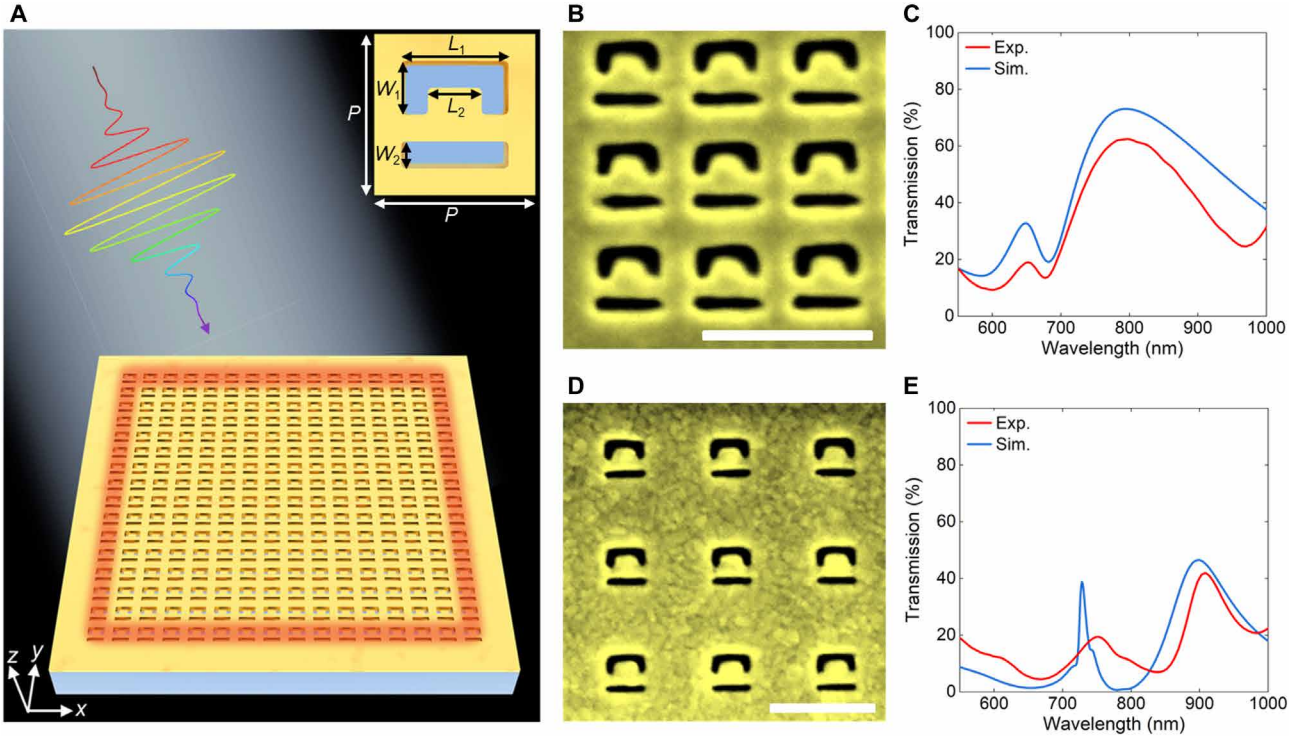

Fig. 1. Optical responses in the bright field. (**A**) Schematic diagram of the dark-field edge emission from nonlocal metasurfaces. Inset is their building block, ASR. Geometric parameters: $L_1 = 200$ nm, $L_2 = 100$ nm, $W_1 = 100$ nm, $W_2 = 50$ nm. (**B**) SEM images of the fabricated sample and (**C**) its experimental and simulated transmission spectra in the bright field with array period $P = 300$ nm. Scale bars, 500 nm. (**D** and **E**) Those for $P = 500$ nm.

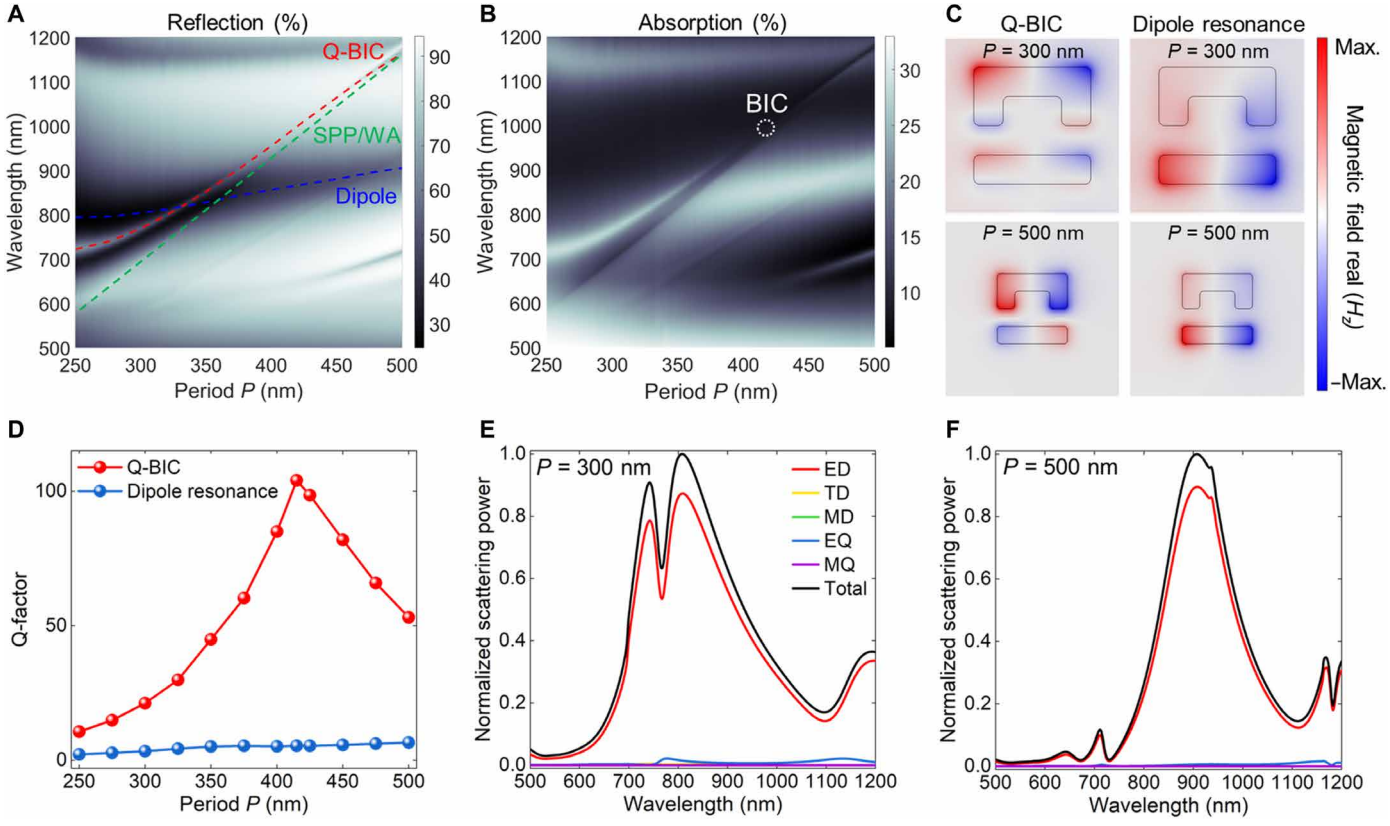

Fig. 2. Design of the ASR in the dark field. (**A**) Simulated reflection and (**B**) absorption spectra as a function of period *P* under TE incidence. Red, green, and blue dashed lines denote q-BIC mode, SPP/WA mode, and dipole resonance, respectively. (**C**) Magnetic field H_z distributions at corresponding resonant wavelengths for periods $P = 300$ and 500 nm. (**D**) Dependences of Q-factors on period *P*. (**E** and **F**) Multipole decompositions of ASRs with periods of 300 and 500 nm. ED, electric dipole; TD, toroidal dipole; MQ, magnetic quadrupole; MD, magnetic dipole; EQ, electric quadrupole; MQ, magnetic quadrupole.

q-BIC, and the Q-factor gradually decreases. The dipole resonance remains relatively uninfluenced by the change of period, showing a slight increase in the Q-factor. This phenomenon indicates that the q-BIC has a large nonlocality while the dipole resonance is local. More details about the analysis of local and nonlocal effects are given in figs. S5 and S11 in the Supplementary Materials.

Because the ASR works in the dark field, the background light will not be collected by the objective. The far-field scattering properties of two ASRs with periods of 300 and 500 nm are investigated by the multipole decompositions method (*10*) in Fig. 2 (E and F). The comparison between simulated scattering power based on multipole theory and the far-field method is presented for verification in fig. S13 in the Supplementary Materials. As shown in Fig. 2E, for period $P = 300$ nm, two resonances approach and strongly couple with each other, resulting in a Fano-like scattering dip at the wavelength of 766 nm, with dominant electric dipole and weak electric quadrupole responses. Compared with the dipole resonance, the q-BIC mode has a larger nonlocality considering the higher Q-factor. Interactions with neighboring units will be absent for the ASR at the metasurface edge. Only the local dipole resonance exists, while the nonlocal q-BIC mode cannot be effectively excited to suppress the scattering, which is beneficial to realize the dark-field edge emission. When period $P = 500$ nm, the overcoupling state cannot suppress the far-field scattering of the dipole resonance, so the local dipole resonance is dominant and all ASRs are expected to have similar scattering in the dark field, which indicates the necessity of combining both local and nonlocal effects. For comparison, the design of a unit with a single slit is shown in fig. S14, indicating the importance of ASR structure for nonlocal effects. The optical responses under TM incidence are also considered. TM wave has a similar response to TE wave. Because the *y*-polarized electric field component is reduced by nearly half for TM wave according to the oblique incident angle of 61°, the excited q-BIC is relatively weak, and the nonlocal responses are mainly contributed by SPP and WA modes with different orders. More details can be found in fig. S8 in the Supplementary Materials.

Because the incident light is oblique, phases of adjacent ASRs are distinct, resulting in the interference of far-field scattering between them. With TE wave incidence, Fig. 3A shows the electric field E_y distributions of two adjacent ASRs with periods of 300 and 500 nm. Two ASRs have positive and negative hotspots, respectively, indicating different and even opposite phases. To investigate the nonlocal effect on the interference, periodic and scattering models are used to approximately simulate the units at and not at the edge, i.e. with and without nonlocal effects, respectively. More simulation details are given in Materials and Methods and section S8 in the Supplementary Materials. Because the scattering intensities of left and right units are the same in the periodic model and have little difference in the scattering model, the intensity after interference is calculated by only considering the influence of phase difference Δφ between two units, which is described as

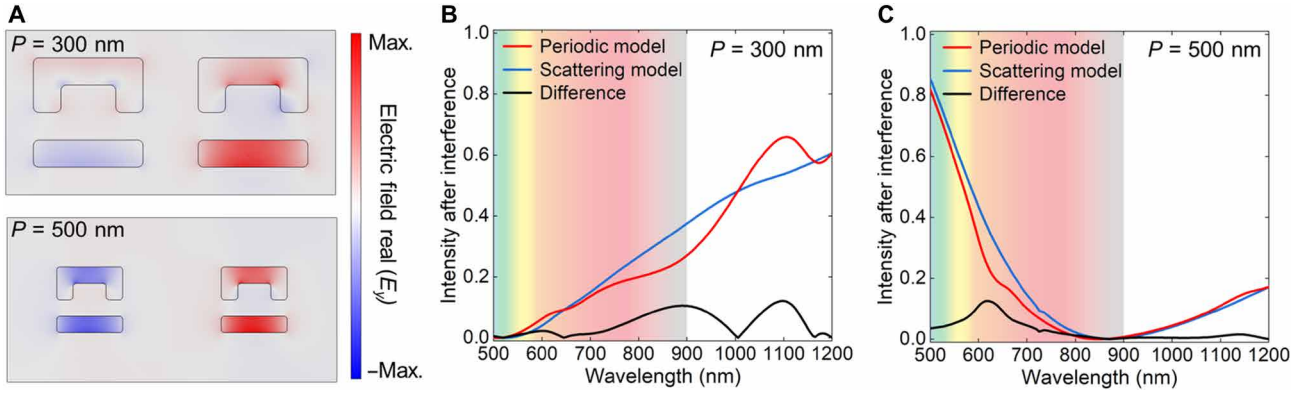

Fig. 3. Interference between adjacent ASRs. (**A**) Electric field E_y distributions of two adjacent ASRs with periods of 300 and 500 nm. (**B** and **C**) Normalized intensity after interference of periodic and scattering models and their differences for two periods. The colored area denotes the wavelength range of the CCD camera.

$$I = \frac{1 + \cos(\Delta\varphi)}{2} \tag{4}$$

Figure 3 (B and C) gives the spectra of intensity after interference for two periods. Because the scattering is dominated by the *y*-component electric dipole moment in multipole decomposition, the phases are extracted from it. More details involving the influence of scattering spectra are shown in fig. S10. The wavelength range of the charge-coupled device (CCD) camera used here is shorter than 900 nm, so the wavelength of 500 to 900 nm (colored area) is considered. In Fig. 3B, the scattering model has a larger intensity after interference for the wavelength of around 700 to 1000 nm and acquires a relatively large difference from that in the periodic model at around 880 nm, which corresponds to the resonant wavelength with a strong scattering in Fig. 2E. The match between wavelengths of effective and strong resonance scattering further enlarges the difference between ASRs at the edge and center. The ASR at the edge can thus provide a larger scattering. For the period of 500 nm, strong scattering emerges at the wavelength of ~900 nm in Fig. 2F, while the intensities after interference of both models are nearly identical near this wavelength in Fig. 3C. Therefore, the resonance response is dominated by the local responses, which are expected to have a similar dark-field emission for units at the center and edge. In addition, TM wave has a similar phenomenon; more details can be found in fig. S9 in the Supplementary Materials.

Dark-field edge emission

To demonstrate the dark-field edge emission of the proposed nonlocal metasurface, Fig. 4 (A and D) shows the dark-field imaging of the 16 × 16 array for periods $P = 300$ and 500 nm. Consistent with the analysis above, edge emission of the metasurface can be observed for period $P = 300$ nm with nonlocal effects, while all units produce similar dark-field scattering for period $P = 500$ nm without nonlocal effects. Figure 4 (B and E) presents their normalized scattering spectra measured by averaging the scattering intensity of all pixels along the *y* direction in the red square and the *x* direction in the green square, respectively. For pixels along the *x* direction with period $P = 300$ nm, the resonance with the largest scattering emerges at the wavelength of ~820 nm, which agrees with the simulation results in Fig. 2E. The resonant wavelength of *y*-direction pixels shows a red shift, and the bandwidth becomes wider, which is due to partial contribution from the TM wave. For period $P = 500$ nm, pixels along the *x* and *y* directions have similar scattering spectra with a resonant wavelength of around 770 nm. The slight blue shift compared with the simulation in Fig. 2F is attributed to the interference between adjacent ASRs, as well as the imperfection and disorder of the sample. Figure 4 (C and F) shows the average scattering spectra of ASRs at and not at the edge, which agrees with the phenomenon in Fig. 4 (A and D). ASRs at the edge have more than twice the scattering intensity of ASRs not at the edge for a period of 300 nm, while their scatterings are similar for a period of 500 nm. The property of edge emission can also be realized for less unit number. More results about different periods and unit numbers are given in figs. S4 and S5 in the Supplementary Materials, which further demonstrate the contributions of nonlocal effects. Compared with conventional local metasurfaces, the proposed nonlocal metasurface requires only one type of meta-atom without additional design of meta-atoms or defects with different scattering properties. It is interesting to point out that besides the local and nonlocal resonances analyzed above, some topological edge states may be involved to enhance the scattering at the edge additionally. Because the practical dark-field incidence condition is complex, the subsequent complicated edge states are not discussed for simplicity.

To further explore the smaller scale of the manipulation of nonlocal effects, Fig. 5 shows the property of dark-field edge emission of random ASR arrangements. Metasurfaces with a central unpatterned square and random unpatterned squares are demonstrated, as shown in the SEM images in Fig. 5 (A and C). Figure 5 (B and D) gives the dark-field imaging of two metasurfaces. It can be seen that not only the property of edge emission remains but also the unpatterned units (colored dashed squares) at the center can generate the strong dark-field emission. The minimal manipulation scale can achieve a 3 × 3 array and even a single unit, showing a higher flexibility for the manipulation of nonlocal effects in the dark field. The flexible spatial scattering modulation achieved by simply erasing some units is difficult to realize by only local responses because the unpatterned units in local metasurfaces generally suppress the scattering. It should be noted that the unpatterned position has an influence on the scattering. The unpatterned units close to the center have larger emissions than those near the edge due to stronger nonlocality and sufficient interference, and those at the edge can thus not provide effective scattering. More details are given in fig. S3 in

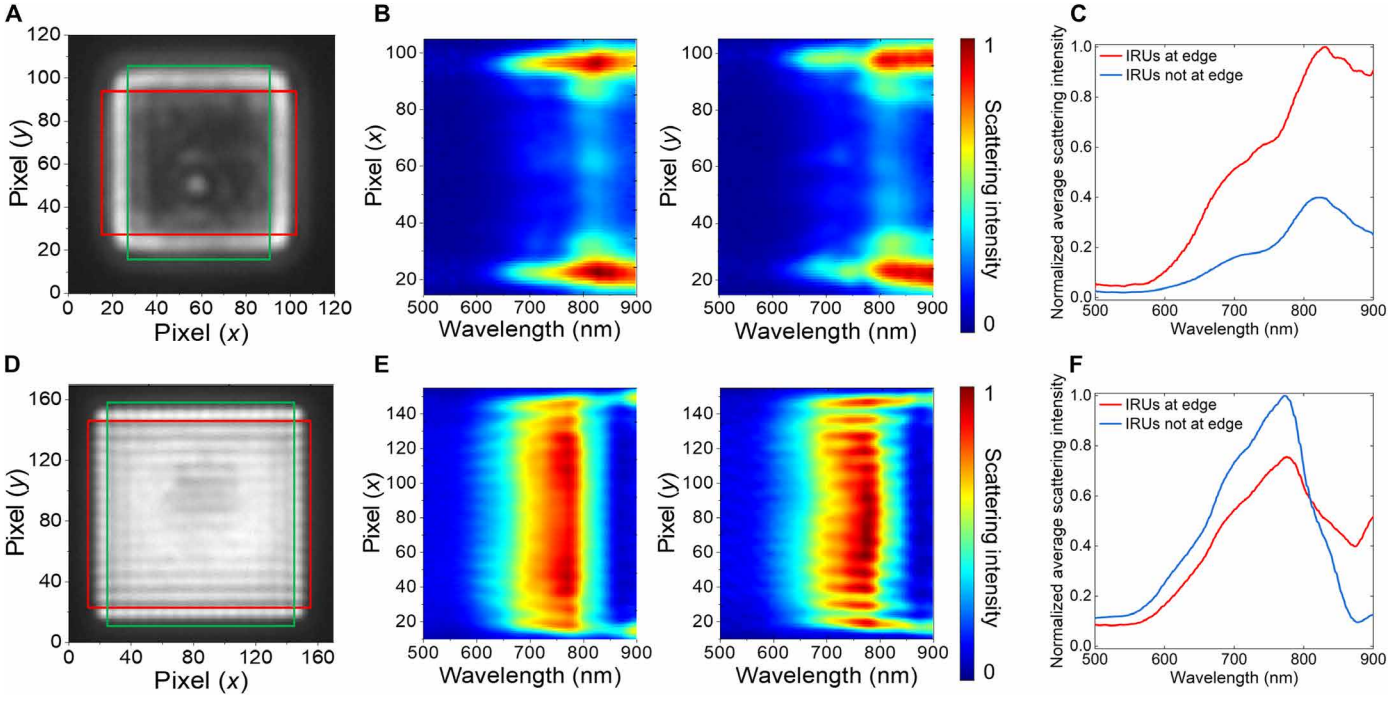

Fig. 4. Dark-field edge emission of the proposed nonlocal metasurface. (**A**) Dark-field imaging and (**B**) normalized scattering spectra for period $P = 300$ nm. Red and green squares denote the sampling positions. Two scattering spectra are measured by averaging the scattering intensity of all pixels along the *y* direction in the red square and the *x* direction in the green square, respectively. (**C**) Average scattering spectra of ASRs at and not at the edge for period $P = 300$ nm. (**D** to **F**) Those for period $P = 500$ nm.

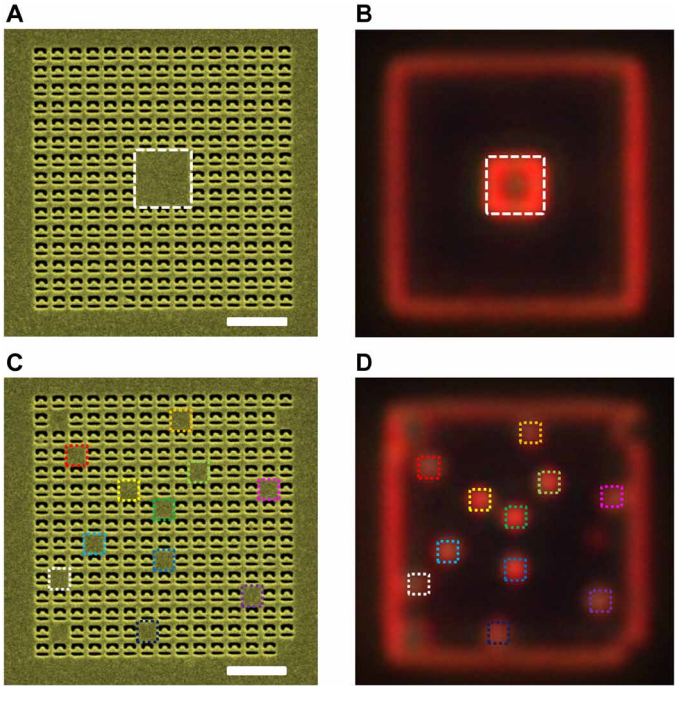

Fig. 5. Dark-field edge emission of random ASR arrangements. (**A**) SEM image and (**B**) dark-field imaging of the metasurface with a central unpatterned square. Colored dashed squares denote the unpatterned positions. (**C** and **D**) Those for the metasurface with random unpatterned squares. Scale bars, 1000 nm.

the Supplementary Materials. Because the optical radiation pressure force is determined by the scattering property, the flexible scattering manipulation in the proposed nonlocal metasurfaces provides the potential in applications of optical trapping and sorting at the nanoscale (*47*–*49*). More details are given in section S12 in the Supplementary Materials.

DISCUSSION

In summary, we have proposed the plasmonic nonlocal metasurfaces and demonstrated their properties of dark-field edge emission. By manipulating the geometric parameter of the array period, local dipole resonances and nonlocal resonances such as q-BIC, SPP, and WA modes can be excited and tailored to produce different scattering properties for ASRs at different positions of the metasurface. Experimental results show that the nonlocal metasurface can achieve the dark-field edge emission and its flexible control up to pixel level. The efficiency and multifunctionality might be enhanced by involving low-loss dielectric materials with multipole Mie-type resonances. The nonlocal metasurface can also involve various local effects designed in local counterparts, providing more peculiar physical mechanisms and functionalities than local metasurfaces. Topology optimization and artificial intelligence are effective tools to optimize the interactions between meta-atoms and thus highly control the nonlocal effect (*50*, *51*). This nonlocal metasurface can be further used in phase-modulated, dynamic, and time-varying metadevices (*52*–*54*). The manipulation of nonlocal effects can enhance the interactions between light and matter and improve the capability of light scattering, which will promote practical applications in nanoscale light trapping and biological sorting.

MATERIALS AND METHODS

Simulation

Electromagnetic responses of ASRs and metasurfaces were numerically simulated using commercial software COMSOL Multiphysics based on the finite element method. Perfectly matched layers (PMLs) were implemented at the top and bottom of the structure to truncate the open space. Periodic boundary conditions were applied in the x and y directions to simulate the periodic model. They were replaced by PMLs for the simulation of the scattering model. Scattering power was calculated on the basis of the multipole decomposition theory. The refractive index of silica substrate is 1.45. The permittivity of gold is from the data measured by Johnson and Christy (*55*), whose imaginary part was doubled to consider the nonradiative loss from the imperfect fabrication.

Fabrication

A 50-nm-thick gold film was deposited on a SiO_2 substrate by thermal evaporation. The metasurface was patterned by a focused ion beam milling system (Helios Nanolab 660 DualBeam) with the operational current of an ion gun of 0.78 pA and an acceleration voltage of 30 kV.

Measurement

The transmittance and the scattering spectra of the structures were investigated by Fourier-based imaging spectroscopy. The acquisition of the hyperspectral data cube was carried out by a commercial imaging spectrometer (SpectraCube by Applied Spectral Imaging, Haifa, Israel) coupled to a microscope (AxioImager Z1.m by Zeiss, Oberkochen, Germany). The scattering spectra were recorded under reflected dark-field illumination. All measurements were performed with a 100× objective (LD EC Epiplan-Neofluar 100×/0.9 BD DIC M27 by Zeiss, Oberkochen, Germany). A linear polarizer was placed between the light source and the sample for the transmission measurements. For measurements in dark-field reflection mode, the polarizer was placed between the light source and the dark-field objective.

To take the different exposure times of the image acquisition into consideration when calculating the transmittance, the transmission spectra of the array were multiplied by the ratio t_{lamp}/t_{sample} where t_{lamp} is the exposure time of the lamp and t_{sample} is the exposure time of the sample. Afterwards, the transmission spectra were normalized on a dark-current corrected lamp spectrum as

$$T = \frac{t_{lamp} I_{sample}}{t_{sample}(I_{lamp} - I_{DC})} \tag{5}$$

where t_{lamp} and t_{sample} are the exposure times used to measure the lamp spectrum and the sample, respectively. I_{sample} represents the power spectrum of the sample. I_{lamp} is the lamp spectrum, and I_{DC} represents the spectrum of the dark current. The transmittance spectra were generated by choosing the region of interest with the ASR array and averaging over all pixels confined in this region.

The raw scattering spectra of the nanostructures were normalized on the incident light spectrum. Afterwards, a region of interest with the ASR array was extracted and the pixels in the square were either projected along one axis or averaged. Another region of interest with no nanostructures was extracted and used to generate the background signal, which was subtracted from the projected or averaged scattering spectra. The scattering spectra are described as

$$S = \frac{I_{array} - I_{BG}}{(I_{lamp} - I_{DC})} \tag{6}$$

where I_{array} represents the power spectrum of the ASR array. I_{BG} is the background spectrum of the gold layer. I_{lamp} is the lamp spectrum, and I_{DC} represents the spectrum of the dark current.

Supplementary Materials

This PDF file includes:

Sections S1 to S12
Figs. S1 to S14
References

REFERENCES AND NOTES

1. X. Luo, Principles of electromagnetic waves in metasurfaces. *Sci. China Phys. Mech.* **58**, 5688 (2015).
2. R. Chai, Q. Liu, W. Liu, Z. Li, H. Cheng, J. Tian, S. Chen, Emerging planar nanostructures involving both local and nonlocal modes. *ACS Photonics* **10**, 2031–2044 (2023).
3. Y. Guo, M. Pu, F. Zhang, M. Xu, X. Li, X. Ma, X. Luo, Classical and generalized geometric phase in electromagnetic metasurfaces. *Photonics Insights* **1**, R03 (2022).
4. N. Meinzer, W. L. Barnes, I. R. Hooper, Plasmonic meta-atoms and metasurfaces. *Nat. Photonics* **8**, 889–898 (2014).
5. K. Koshelev, Y. Kivshar, Dielectric resonant metaphotonics. *ACS Photonics* **8**, 102–112 (2021).
6. S. Wang, P. C. Wu, V.-C. Su, Y.-C. Lai, M.-K. Chen, H. Y. Kuo, B. H. Chen, Y. H. Chen, T.-T. Huang, J.-H. Wang, R.-M. Lin, C.-H. Kuan, T. Li, Z. Wang, S. Zhu, D. P. Tsai, A broadband achromatic metalens in the visible. *Nat. Nanotechnol.* **13**, 227–232 (2018).
7. J. Yao, M. K. Chen, R. Lin, D. P. Tsai, K. M. Luk, Tunable Water-Based Meta-Lens. *Opt. Mater.* **12**, 2300130 (2024).
8. J. C. Zhang, G.-B. Wu, M. K. Chen, X. Liu, K. F. Chan, D. P. Tsai, C. H. Chan, A 6G meta-device for 3D varifocal. *Sci. Adv.* **9**, eadf8478 (2023).
9. H. Altug, S.-H. Oh, S. A. Maier, J. Homola, Advances and applications of nanophotonic biosensors. *Nat. Nanotechnol.* **17**, 5–16 (2022).
10. J. Yao, J.-Y. Ou, V. Savinov, M. K. Chen, H. Y. Kuo, N. I. Zheludev, D. P. Tsai, Plasmonic anapole metamaterial for refractive index sensing. *PhotoniX* **3**, 23 (2022).
11. J. C. Zhang, M. K. Chen, Y. Liang, X. Hong, M. Wang, Y. Cheng, X. Liu, D. P. Tsai, S. W. Pang, Nanoimprint Meta-Device for Chiral Imaging. *Adv. Funct. Mater.* **33**, 2306422 (2023).
12. M. K. Chen, X. Y. Liu, Y. F. Wu, J. C. Zhang, J. Q. Yuan, Z. N. Zhang, D. P. Tsai, A Meta-Device for Intelligent Depth Perception. *Adv. Mater.* **35**, e2107465 (2023).
13. M. L. Tseng, M. Semmlinger, M. Zhang, C. Arndt, T. T. Huang, J. Yang, H. Y. Kuo, V. C. Su, M. K. Chen, C. H. Chu, B. Cerjan, D. P. Tsai, P. Nordlander, N. J. Halas, Vacuum ultraviolet nonlinear metalens. *Sci. Adv.* **8**, eabn5644 (2022).
14. L. Li, Z. X. Liu, X. F. Ren, S. M. Wang, V. C. Su, M. K. Chen, C. H. Chu, H. Y. Kuo, B. H. Liu, W. B. Zang, G. C. Guo, L. J. Zhang, Z. L. Wang, S. N. Zhu, D. P. Tsai, Metalens-array–based high-dimensional and multiphoton quantum source. *Science* **368**, 1487–1490 (2020).
15. Y. Fan, H. Liang, J. Li, D. P. Tsai, S. Zhang, Emerging Trend in Unconventional Metasurfaces: From Nonlinear, Non-Hermitian to Nonclassical Metasurfaces. *ACS Photonics* **9**, 2872–2890 (2022).
16. Y. Fan, H. Liang, Y. Wang, S. Chen, F. Lai, M. Ku Chen, S. Xiao, J. Li, D. P. Tsai, Dual-channel quantum meta-hologram for display. *Adv. Photonics Nexus* **3**, 016011 (2024).
17. Y. Liang, D. P. Tsai, Y. Kivshar. From local to nonlocal high-Q plasmonic metasurfaces. arXiv:2311.13452 [physics.optics] (22 November 2023).
18. V. Fedotov, M. Rose, S. Prosvirnin, N. Papasimakis, N. Zheludev, Sharp trapped-mode resonances in planar metamaterials with a broken structural symmetry. *Phys. Rev. Lett.* **99**, 147401 (2007).
19. V. A. Fedotov, N. Papasimakis, E. Plum, A. Bitzer, M. Walther, P. Kuo, D. Tsai, N. Zheludev, Spectral collapse in ensembles of metamolecules. *Phys. Rev. Lett.* **104**, 223901 (2010).
20. K. Shastri, F. Monticone, Nonlocal flat optics. *Nat. Photonics* **17**, 36–47 (2023).
21. J. Yao, R. Lin, M. K. Chen, D. P. Tsai, Integrated-resonant metadevices: A review. *Adv. Photonics* **5**, 024001 (2023).
22. J. Yao, Y. Chen, L. Ye, N. Liu, G. Cai, Q. H. Liu, Multiple resonant excitations of surface plasmons in a graphene stratified slab by Otto configuration and their independent tuning. *Photonics Res.* **5**, 377–384 (2017).
23. Q. Xu, Y. Lang, X. Jiang, X. Yuan, Y. Xu, J. Gu, Z. Tian, C. Ouyang, X. Zhang, J. Han, Meta-optics inspired surface plasmon devices. *Photonics Insights* **2**, R02 (2023).
24. K. V. Sreekanth, J. Perumal, U. Dinish, P. Prabhathan, Y. Liu, R. Singh, M. Olivo, J. Teng, Tunable Tamm plasmon cavity as a scalable biosensing platform for surface enhanced resonance Raman spectroscopy. *Nat. Commun.* **14**, 7085 (2023).

25. A. Bitzer, J. Wallauer, H. Helm, H. Merbold, T. Feurer, M. Walther, Lattice modes mediate radiative coupling in metamaterial arrays. *Opt. Express* **17**, 22108–22113 (2009).
26. M. S. Bin-Alam, O. Reshef, Y. Mamchur, M. Z. Alam, G. Carlow, J. Upham, B. T. Sullivan, J.-M. Ménard, M. J. Huttunen, R. W. Boyd, Ultra-high-Q resonances in plasmonic metasurfaces. *Nat. Commun.* **12**, 974 (2021).
27. L. Huang, R. Jin, C. Zhou, G. Li, L. Xu, A. Overvig, F. Deng, X. Chen, W. Lu, A. Alù, Ultrahigh-Q guided mode resonances in an All-dielectric metasurface. *Nat. Commun.* **14**, 3433 (2023).
28. M. Lawrence, D. Barton III, J. Dixon, J. H. Song, J. van de Groep, M. L. Brongersma, J. A. Dionne, High quality factor phase gradient metasurfaces. *Nat. Nanotechnol.* **15**, 956–961 (2020).
29. J. Zhang, J. Ma, M. Parry, M. Cai, R. Camacho-Morales, L. Xu, D. N. Neshev, A. A. Sukhorukov, Spatially entangled photon pairs from lithium niobate nonlocal metasurfaces. *Sci. Adv.* **8**, eabq4240 (2022).
30. M. Sharma, M. Tal, C. McDonnell, T. Ellenbogen, Electrically and all-optically switchable nonlocal nonlinear metasurfaces. *Sci. Adv.* **9**, eadh2353 (2023).
31. X. Wang, T. Sentz, S. Bharadwaj, S. K. Ray, Y. Wang, D. Jiao, L. Qi, Z. Jacob, Observation of nonvanishing optical helicity in thermal radiation from symmetry-broken metasurfaces. *Sci. Adv.* **9**, eade4203 (2023).
32. A. Silva, F. Monticone, G. Castaldi, V. Galdi, A. Alù, N. Engheta, Performing mathematical operations with metamaterials. *Science* **343**, 160–163 (2014).
33. J.-H. Song, J. van de Groep, S. J. Kim, M. L. Brongersma, Non-local metasurfaces for spectrally decoupled wavefront manipulation and eye tracking. *Nat. Nanotechnol.* **16**, 1224–1230 (2021).
34. A. C. Overvig, S. C. Malek, N. Yu, Multifunctional nonlocal metasurfaces. *Phys. Rev. Lett.* **125**, 017402 (2020).
35. X. Xie, M. Pu, J. Jin, M. Xu, Y. Guo, X. Li, P. Gao, X. Ma, X. Luo, Generalized Pancharatnam-Berry phase in rotationally symmetric meta-atoms. *Phys. Rev. Lett.* **126**, 183902 (2021).
36. S. C. Malek, A. C. Overvig, A. Alu, N. Yu, Multifunctional resonant wavefront-shaping meta-optics based on multilayer and multi-perturbation nonlocal metasurfaces. *Light: Sci. Appl.* **11**, 246 (2022).
37. J. Yao, R. Lin, X. Che, Y. Fan, Y. Liang, J. Zhang, M. K. Chen, D. P. Tsai, Integrated-Resonant Units for Phase Compensation and Efficiency Enhancements in Achromatic Meta-lenses. *ACS Photonics* **10**, 4273–4281 (2023).
38. K. Koshelev, S. Lepeshov, M. Liu, A. Bogdanov, Y. Kivshar, Asymmetric metasurfaces with high-Q resonances governed by bound states in the continuum. *Phys. Rev. Lett.* **121**, 193903 (2018).
39. Y. Liang, K. Koshelev, F. Zhang, H. Lin, S. Lin, J. Wu, B. Jia, Y. Kivshar, Bound states in the continuum in anisotropic plasmonic metasurfaces. *Nano Lett.* **20**, 6351–6356 (2020).
40. Y. Tang, Y. Liang, J. Yao, M. K. Chen, S. Lin, Z. Wang, J. Zhang, X. G. Huang, C. Yu, D. P. Tsai, Chiral Bound States in the Continuum in Plasmonic Metasurfaces. *Laser Photonics Rev.* **17**, 2200597 (2023).
41. X. Zhang, Y. Liu, J. Han, Y. Kivshar, Q. Song, Chiral emission from resonant metasurfaces. *Science* **377**, 1215–1218 (2022).
42. J. Fan, Z. Li, Z. Xue, H. Xing, D. Lu, G. Xu, J. Gu, J. Han, L. Cong, Hybrid bound states in the continuum in terahertz metasurfaces. *Opto-Electron. Sci.* **2**, 230006 (2023).
43. S. D. Jenkins, J. Ruostekoski, N. Papasimakis, S. Savo, N. I. Zheludev, Many-body subradiant excitations in metamaterial arrays: Experiment and theory. *Phys. Rev. Lett.* **119**, 053901 (2017).
44. A. Xomalis, I. Demirtzioglou, E. Plum, Y. Jung, V. Nalla, C. Lacava, K. F. MacDonald, P. Petropoulos, D. J. Richardson, N. I. Zheludev, Fibre-optic metadevice for all-optical signal modulation based on coherent absorption. *Nat. Commun.* **9**, 182 (2018).
45. M. Papaioannou, E. Plum, E. T. Rogers, N. I. Zheludev, All-optical dynamic focusing of light via coherent absorption in a plasmonic metasurface. *Light: Sci. Appl.* **7**, 17157 (2018).
46. Y. Shen, J. Zhou, T. Liu, Y. Tao, R. Jiang, M. Liu, G. Xiao, J. Zhu, Z.-K. Zhou, X. Wang, Plasmonic gold mushroom arrays with refractive index sensing figures of merit approaching the theoretical limit. *Nat. Commun.* **4**, 2381 (2013).
47. J. Zhang, K. F. MacDonald, N. I. Zheludev, Giant optical forces in planar dielectric photonic metamaterials. *Opt. Lett.* **39**, 4883–4886 (2014).
48. T. Liu, J.-Y. Ou, K. F. MacDonald, N. I. Zheludev, Photonic metamaterial analogue of a continuous time crystal. *Nat. Phys.* **19**, 986–991 (2023).
49. Y. Y. Tanaka, P. Albella, M. Rahmani, V. Giannini, S. A. Maier, T. Shimura, Plasmonic linear nanomotor using lateral optical forces. *Sci. Adv.* **6**, eabc3726 (2020).
50. M. Xu, Q. He, M. Pu, F. Zhang, L. Li, D. Sang, Y. Guo, R. Zhang, X. Li, X. Ma, X. Luo, Emerging Long-Range Order from a Freeform Disordered Metasurface. *Adv. Mater.* **34**, e2108709 (2022).
51. M. K. Chen, X. Liu, Y. Sun, D. P. Tsai, Artificial Intelligence in Meta-optics. *Chem. Rev.* **122**, 15356–15413 (2022).
52. A. Overvig, A. Alù, Diffractive nonlocal metasurfaces. *Laser Photonics Rev.* **16**, 2100633 (2022).
53. D. Papas, J. Y. Ou, E. Plum, N. I. Zheludev, Microwatt volatile optical bistability via nanomechanical nonlinearity. *Adv. Sci.* **10**, e2300042 (2023).
54. R. Tirole, S. Vezzoli, E. Galiffi, I. Robertson, D. Maurice, B. Tilmann, S. A. Maier, J. B. Pendry, R. Sapienza, Double-slit time diffraction at optical frequencies. *Nat. Phys.* **19**, 999–1002 (2023).
55. P. B. Johnson, R.-W. Christy, Optical constants of the noble metals. *Phys. Rev. B* **6**, 4370–4379 (1972).
56. A. Ashkin, Acceleration and trapping of particles by radiation pressure. *Phys. Rev. Lett.* **24**, 156–159 (1970).
57. M. Riccardi, O. J. Martin, Electromagnetic forces and torques: From dielectrophoresis to optical tweezers. *Chem. Rev.* **123**, 1680–1711 (2023).
58. H. Luo, X. Fang, C. Li, X. Dai, N. Ru, M. You, T. He, P. C. Wu, Z. Wang, Y. Shi, X. Cheng, 1 Nm-resolution sorting of sub-10 Nm nanoparticles using a dielectric metasurface with toroidal responses. *Small Sci.* **3**, 2300100 (2023).

Acknowledgments

Funding: This work is supported by the University Grants Committee / Research Grants Council of the Hong Kong Special Administrative Region, China (project no. AoE/P-502/20, CRF Project: C1015-21E; C5031-22G; and GRF Project: CityU15303521; CityU11305223; CityU11310522; CityU11300123), the Department of Science and Technology of Guangdong Province (project no. 2020B1515120073), City University of Hong Kong (project nos. 9380131, 9610628, and 7005867), and the National Natural Science Foundation of China (project no. 62375232). **Author contributions:** J.Y., M.K.C., and D.P.T. conceived the idea and designed the experiments. J.Y. designed the samples and performed the theoretical simulations. W.-L.H. performed sample fabrications and optical measurements. J.Y., Y.L., and M.K.C. performed the data analysis. J.Y. prepared the manuscript, and all authors reviewed it. M.K.C. and D.P.T. initiated and supervised the research. **Competing interests:** The authors declare that they have no competing interests. **Data and materials availability:** All data needed to evaluate the conclusions in the paper are present in the paper and/or the Supplementary Materials.

Submitted 2 December 2023
Accepted 13 March 2024
Published 17 April 2024
10.1126/sciadv.adn2752